Journal of the Optical Society of America B
OPTICAL PHYSICS

Synthetic Lorentz force in an expanding cold atomic gas

N. Šantić,[1,2,*] T. Dubček,[2] D. Aumiler,[1] H. Buljan,[2] and T. Ban[1]

[1]Institute of Physics, Bijenička c. 46, 10000 Zagreb, Croatia
[2]Department of Physics, University of Zagreb, Bijenička c. 32, 10000 Zagreb, Croatia
*Corresponding author: nsantic@ifs.hr

Received 15 February 2017; revised 27 April 2017; accepted 29 April 2017; posted 3 May 2017 (Doc. ID 286769); published 26 May 2017

We implement a synthetic Lorentz force in a cold atomic gas released from a magneto-optical trap. The signature of this is an angular deflection of a rotationally asymmetrical cloud. The effect is a consequence of thermal expansion of the cold atomic cloud under the influence of the applied synthetic Lorentz force. The synthetic Lorentz force is based on radiation pressure and the Doppler effect, making it straightforward to implement. The introduction of synthetic magnetism into our system, together with the fact that it is readily described by the Fokker–Planck equation, makes it an excellent candidate to emulate numerous complex classical systems.

OCIS codes: (020.3320) Laser cooling; (020.0020) Atomic and molecular physics.

https://doi.org/10.1364/JOSAB.34.001264

1. INTRODUCTION

Radiation trapping in cold atomic gases is a known and well-studied effect [1] which sets an upper limit on achievable atom densities in a magneto-optical trap (MOT). The re-absorption of scattered photons in dense atomic clouds gives rise to an effective long-range repulsive force between atoms that scales as $1/r^2$, analogous to the Coulomb force between charges. Consequently, it is possible to assign an effective (synthetic) charge to the atoms [2], and tune its value by changing the intensity and detuning of the scattered radiation. This also offers the possibility of realizing a time-dependent synthetic charge, a regime not accessible with real charges in electrodynamics.

The analogy between clouds of cold atoms and plasmas has led to the observation of Coulomb explosion in expanding molasses [3], to the prediction of plasma-acoustic waves [4], and many other plasma-like phenomena [5–9]. In addition, equations of equilibrium governing the atomic distribution in a dense atomic cloud are similar to the equation of hydrostatic equilibrium in stars, experimentally demonstrated in [10], with the trapping force having replaced gravity. This led to the observation of self-sustained oscillations in a MOT [11], analogous to oscillations in stars. Consequently, it is reasonable to consider a dense cloud of cold atoms in a MOT as an ideal classical emulator that could simulate complex classical systems, for example a tokamak fusion reactor or astrophysical objects, such as stars and globular clusters. However, since magnetism plays a key role in the aforementioned systems, in order to achieve this goal it is necessary to introduce synthetic magnetism in the classical system of cold atoms in a MOT.

Apart from our recent work [12], all up-to-date realizations of synthetic magnetism involved ultra-cold, quantum degenerate atomic gases: Bose–Einstein condensates (BECs) and Fermi degenerated gases. Experiments implementing such systems hold potential to be used as quantum emulators of strongly correlated many-body systems. The introduction of synthetic magnetism to these experiments has enabled realization of many interesting phenomena, ranging from the Hall effect [13] to the experimental realization of the Hofstadter Hamiltonian [14], and has initiated a new and attractive research direction. For recent reviews see [15,16]. Early realizations of synthetic magnetism in ultra-cold atomic systems employed the analogy between the Coriolis force and the Lorentz force by rotating the BEC [17,18]. More recent experiments, both in bulk BECs [19] and optical lattices [20], use laser–atom interactions and employ the analogy between the Berry phase and the Aharonov–Bohm phase. However, methods relying on the Berry phase analogy used in BECs are not applicable for high atom velocities and large cloud volumes found in a MOT.

We use a different method to introduce a synthetic Lorentz force (SLF) to a classical system of cold atoms. It is based on radiation pressure and the Doppler effect, and was introduced theoretically in our recent paper [21]. Using radiation pressure is necessarily accompanied by spontaneous emission and radiation trapping, which makes our method non-applicable to quantum degenerate systems. However, atomic samples prepared in a MOT, still classical and relatively hot to those in BECs, are not significantly affected by the additional heating introduced by spontaneous emission. Moreover, the radiation

trapping which accompanies spontaneous emission is, as discussed above, the basis for the analogy between clouds of cold atoms and classical systems of charged particles such as plasmas.

Two scenarios for the observation of the SLF were proposed in [21], each characterized with a completely different initial velocity distribution of cold atoms and each suitable for emulation of different classical systems.

The first scenario is suitable for the emulation of a single charged particle in a magnetic field, and was experimentally demonstrated in our recent work [12]. We first prepared a cloud with a given center-of-mass (CM) velocity, after which we measured trajectories of the CM of the atomic cloud in the presence of the SLF for various initial CM velocities. The observed trajectories of the CM of the atomic cloud can be interpreted as dynamics of a single charged particle under the influence of the Lorentz force, suggesting approximately equal SLF for all atoms in the cloud, due to the equal initial velocities.

The second scenario is experimentally demonstrated in this work. The cold cloud is considered as an ensemble of particles with a Maxwell–Boltzmann velocity distribution. The signature of the SLF is observed in the shape of the expanding cloud, i.e., an asymmetric and tilted expanding cloud is observed. Our system, a dense atomic cloud in a MOT, is analogous to an expanding single species plasma in a magnetic field, also to an expanding neutral gas in a rotating frame under the influence of a Coriolis force, for instance, an anticyclone. Just as experiments with quantum degenerate gases benefited from the introduction of synthetic magnetism, experiments mimicking classical systems with electrical charges would benefit from the introduction of a SLF in a dense cloud of cold atoms in a MOT. Therefore, our work provides the final missing ingredient needed for the realization of an emulator of complex classical systems whose behavior cannot yet be understood by use of computer simulations [22].

For the purpose of this work, we have upgraded the basic idea presented in [12] and developed a modified experimental setup. A SLF is implemented in the experiment by introducing two pairs of perpendicular laser beams into a system of five-level atoms. Each pair drives two-step two-photon transitions between three levels, from the same ground state but to different exited states, see Figs. 1(a) and 1(b). One pair of perpendicular laser beams, depicted with arrows with solid color filling, drives the $|0\rangle \rightarrow |1\rangle \rightarrow |2\rangle$ transition, while the other pair, marked with pattern filling, drives the $|0\rangle \rightarrow |1'\rangle \rightarrow |2'\rangle$ transition. Due to the Doppler effect and the geometry of the laser beams, both components of the radiation pressure force depend on both components of the atom velocity: $F_x = F_x(v_x, v_y)$ and $F_y = F_y(v_x, v_y)$. This gives us the opportunity to choose the detuning values of our lasers such that the radiation pressure force mimics the Lorentz force, e.g., F_y is positive/negative for atoms with a negative/positive velocity component v_x and the total force is zero for an atom at rest $F(\mathbf{v} = 0) = 0$. In Figs. 1(c) and 1(d) we show the calculated force components F_x and F_y as a function of atom velocities for the system and laser detunings used in the experiment. This force pattern in velocity space can be separated in to two components, one that results in a scalar potential in velocity space and the other that

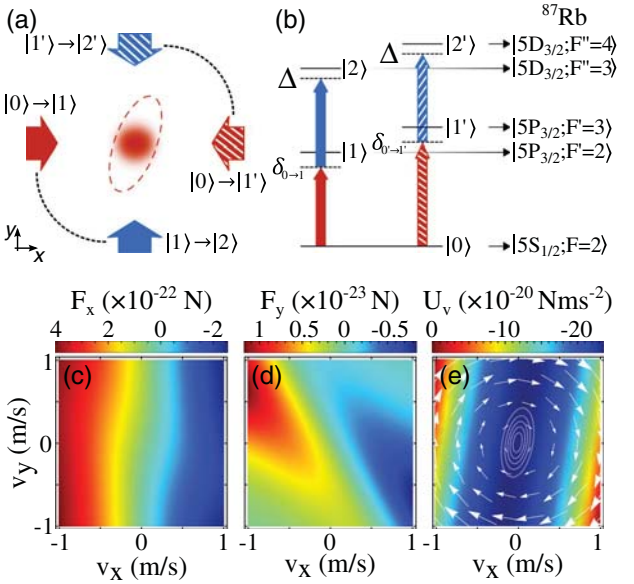

Fig. 1. Scheme for obtaining the synthetic Lorentz force and the resulting force patterns in velocity space. (a) The four beams responsible for the SLF. They propagate in the xy plane (horizontal). The red beams counterpropagating along the x-axis couple states $|0\rangle \rightarrow |1\rangle/|1'\rangle$ (solid/dashed) while the two blue beams counterpropagating along the y-axis couple states $|1\rangle/|1'\rangle \rightarrow |2\rangle/|2'\rangle$ (solid/dashed). (b) The hyperfine levels used for the realization of the SLF. (c) The calculated force in the x and (d) y direction as a function of velocity. (e) Resulting potential in velocity space when the rotating part of the force (shown with white arrows) is excluded. The white contours show the calculated velocity distribution after 1 ms of expansion.

rotates and is responsible for the SLF. The resulting scalar potential, along with the rotating part of the force, is shown in Fig. 1(e). These two components will both influence the observed shape of the cloud. A detailed explanation of the numerical calculations and of the contributions of the two force components in velocity space is given in Section 3. In contrast to the previous experimental realization [12] where three different levels were used, in this work we use five different levels. Using three different levels results in a similar force pattern in velocity space; however, the force is not symmetric, i.e., F_y has different magnitudes for positive and negative v_x of the same magnitude. Using five levels avoids this problem resulting in a better analogy with the Lorentz force and is adequate for experiments in which a symmetrical initial velocity distribution is used.

2. EXPERIMENT

The experiment is based on a ^{87}Rb MOT. The cold cloud of approximately 10^8 atoms is loaded from background vapor in a glass cell. The MOT is arranged in a standard three-beam retroreflected configuration which together with the anti-Helmholtz produced quadrupole magnetic field create the trapping potential.

For the SLF we use the geometry sketched out in Fig. 1(a) where the xy plane is the horizontal one. Beams propagating along the x direction drive the first step of our two-step scheme, where for $|0\rangle \rightarrow |1\rangle$ we use the $|5S_{1/2}; F = 2\rangle$

$\rightarrow |5P_{3/2}; F' = 2\rangle$ transition and for $|0\rangle \rightarrow |1'\rangle$ we use the $|5S_{1/2}; F = 2\rangle \rightarrow |5P_{3/2}; F' = 3\rangle$ transition. Beams propagating along the y direction drive the second step of the two-step excitation, where for $|1\rangle \rightarrow |2\rangle$ we use the $|5P_{3/2}; F' = 2\rangle \rightarrow |5D_{5/2}; F'' = 3\rangle$ transition and for $|1'\rangle \rightarrow |2'\rangle$ we use the $|5P_{3/2}; F' = 3\rangle \rightarrow |5D_{5/2}; F'' = 4\rangle$ transition.

The four SLF beams are provided from the output of two frequency stabilized external cavity diode lasers (ECDLs) with nominal emission at 780 nm for the first step and 776 nm for the second step. The ECDL at 780 nm is stabilized using a dither technique to a saturation spectroscopy signal obtained from room temperature rubidium vapor. The ECDL at 776 nm is also stabilized using the dither technique to a Doppler-free two-photon signal obtained from heated rubidium vapor. Using heterodyne spectroscopy with an optical frequency comb, a laser linewidth of 1 MHz is measured. All beams are passed through acousto-optic modulators to obtain the desired frequencies.

Since one of the two-step two-photon pathways drives an open transition, the presence of a repumper is necessary. For this we drive the $|5S_{1/2}; F = 1\rangle \rightarrow |5P_{3/2}; F' = 1\rangle$ transition. Compared to normal MOT conditions the population in the $|5S_{1/2}; F = 1\rangle$ will be substantial leading to an appreciable radiation pressure force from the repumper beam. To avoid masking the observation of the SLF by introducing unaccounted forces into the system we copropagate the repumper beam with the $|5S_{1/2}; F = 2\rangle \rightarrow |5P_{3/2}; F' = 2\rangle$ beam.

Fluorescent imaging is performed along the z-axis, perpendicular to the xy plane in which the four beams driving two two-step two-photon transitions propagate. Gravitational force acts along the z-axis and therefore has no effect on atomic motion in the xy plane. An experimental protocol that is typical for time-of-flight measurements (TOF) is used, with the difference that all four SLF beams are present in the system throughout the experiment cycle. It is important to note here that the SLF beams have no effect on the initial spatial and velocity distributions of the cloud while the trapping beams are present since the force arising from their absorption is small compared to forces due to the trapping beams. The experiment cycle is as follows: (i) we load the cloud, (ii) at $t = 0$ we switch off the trapping beams and the quadrupole magnetic field and the cloud evolves in the presence of the synthetic Lorentz and Doppler forces induced by the SLF beams, (iii) after given expansion time τ we turn on the trapping beams and image the cloud fluorescence. We repeat the measurement protocol 20 times in identical conditions, and subsequently average to obtain the density distribution of the cloud for a given τ.

The following detuning values are chosen in the experiment: the first-step beams, propagating along the x direction, are red detuned by $\delta_{0\rightarrow 1} = \delta_{0\rightarrow 1'} = -\Gamma_P/2$, where $\Gamma_P = 2\pi \times 6.1$ MHz is the decay rate of the ^{87}Rb$5P_{3/2}$ state [23]. The second-step beams, propagating along the y direction, are blue detuned. Their detuning values, $\delta_{1\rightarrow 2}$ and $\delta_{1'\rightarrow 2'}$, are chosen in such a way that the total two-photon detuning, Δ, for both two-photon two-step pathways is equal to $\Delta = -\Gamma_D/2$, where $\Gamma_D = 2\pi \times 0.66$ MHz is the decay rate of the ^{87}Rb$5D_{5/2}$ state [24]. Following this condition, $\delta_{1\rightarrow 2} = \delta_{1'\rightarrow 2'} = 2\pi \times 2.7$ MHz. The repumper laser is on resonance. The choice of those detuning values follows from our recent theoretical paper [21], and is such that we achieve the maximum deflection angle.

Intensities of the SLF beams are: $I_{0\rightarrow 1} = 0.039$ mW/cm^2, $I_{0\rightarrow 1'} = 0.063$mW/cm^2, $I_{1\rightarrow 2} = 3.18$ mW/cm^2, and $I_{1'\rightarrow 2'} = 0.063$ mW/cm^2. The intensity of the repumper beam is $I_{\text{repumper}} = 3.2$ mW/cm^2. All beams are fiber coupled and polarized in the z direction. For the reasons discussed earlier, the repumper beam is coupled to the same fiber as the $|0\rangle \rightarrow |1\rangle$ beam. The offset in the force in the x direction, coming from the repumper radiative force, is compensated with a lower intensity of the $|0\rangle \rightarrow |1\rangle$ beam relative to a case in which the repumper would not be present. In such a way we achieved that the total force on atoms with zero velocity is zero, i.e., $F_x(v = 0) = 0$. As a consequence the SLF will be of lower magnitude but will have the same characteristics.

3. NUMERICAL SIMULATIONS

To be able to analyze the TOF experimental results, first we turn to numerical simulations of our system.

The force in velocity space is calculated by using the density matrix formalism and applying the Ehrenfest theorem [25]. The procedure assumes that the lasers are perfectly monochromatic. However, there is a finite laser linewidth in the experiment that should be taken into account. Considering that the spectral profile of diode lasers can be described by a Gaussian in the frequency domain, we introduce the laser linewidth in the simulations by convolving the force in velocity space with a Gaussian whose FWHM corresponds to the measured laser linewidth, i.e., to 1 MHz. Calculated resulting forces F_x and F_y as a function of atom velocities for relevant rubidium atomic levels and laser parameters used in the experiment are shown in Figs. 1(c) and 1(d). The repumper laser is also included in the calculations.

One can see from Fig. 1(d) that the obtained force pattern has the wanted properties: F_y is positive/negative for atoms with a negative/positive velocity component v_x. Positive F_y arises as a result of driving the $|0\rangle \rightarrow |1\rangle \rightarrow |2\rangle$ transition, by the laser beam pair marked with solid filling in Fig. 1(a). Due to the red-detuned first-step laser driving the $|0\rangle \rightarrow |1\rangle$ transition, this two-step two-photon pathway is resonant only for atoms with negative v_x. The positive force in the $+y$ direction is then a consequence of the second-step laser beam driving the $|1\rangle \rightarrow |2\rangle$ transition. In a completely analogous way, a negative F_y arises as a result of driving $|0\rangle \rightarrow |1'\rangle \rightarrow |2'\rangle$ transition, which is resonant only for atoms with positive v_x.

For sufficiently small velocities the force is linear around zero; therefore, a good approximation is to neglect higher-order terms considering the low atom velocities in a MOT. We Taylor expand the force in velocity up to the linear term:

$$\begin{bmatrix} F_x \\ F_y \end{bmatrix} = \begin{bmatrix} F_{x0} \\ F_{y0} \end{bmatrix} + \begin{bmatrix} \alpha_{xx} & \alpha_{xy} \\ \alpha_{yx} & \alpha_{yy} \end{bmatrix} \begin{bmatrix} v_x \\ v_y \end{bmatrix}. \quad (1)$$

The second term on the right-hand side can be divided into two terms, one that has zero curl in velocity space, while the other rotates:

$$\begin{bmatrix}\alpha_{xx} & \alpha_{xy}\\ \alpha_{yx} & \alpha_{yy}\end{bmatrix}\begin{bmatrix}v_x\\ v_y\end{bmatrix} = \left(\begin{bmatrix}\alpha_{xx} & \alpha_D\\ \alpha_D & \alpha_{yy}\end{bmatrix} + \begin{bmatrix}0 & \alpha_R\\ -\alpha_R & 0\end{bmatrix}\right)\begin{bmatrix}v_x\\ v_y\end{bmatrix}$$
$$= \boldsymbol{F}_{\text{pot}}(\boldsymbol{v}) + \boldsymbol{F}_{SL}(\boldsymbol{v}), \quad (2)$$

where $\alpha_{xy} = \alpha_D + \alpha_R$ and $\alpha_{yx} = \alpha_D - \alpha_R$. We identify the second term $\boldsymbol{F}_{SL}(\boldsymbol{v})$ as the one responsible for the SLF. The first term $\boldsymbol{F}_{\text{pot}}(\boldsymbol{v})$ depends on both components of the atom velocity, and includes the usual Doppler force through the α_{xx} and α_{yy} diagonal terms. Since $\nabla_v \times \boldsymbol{F}_{\text{pot}}(\boldsymbol{v}) = 0$ we can calculate the corresponding potential in velocity space from $\boldsymbol{F}_{\text{pot}} = -\nabla_v U(v_x, v_y)$, where $\nabla_v = \hat{\boldsymbol{v}}_x \partial/\partial v_x + \hat{\boldsymbol{v}}_y \partial/\partial v_y$. It is a two-dimensional angled valley-like potential of the form $U(v_x, v_y) = \alpha_{xx} v_x^2/2 + \alpha_D v_x v_y + \alpha_{yy} v_y^2/2$. In Fig. 1(e), we present the calculated potential, together with the direction and magnitude of the $\boldsymbol{F}_{SL}(\boldsymbol{v})$ force, given by the white arrows. Consider now how these two terms affect the atomic velocity distribution. We start with a symmetric velocity distribution at $t = 0$, which is a common initial condition in a MOT. Shortly after $t = 0$ the cloud will be reshaped in velocity space to a tilted ellipsoid by the potential shown in Fig. 1(e). Simultaneously, the rotating part of the force, $\boldsymbol{F}_{SL}(\boldsymbol{v})$ increases the distribution's deflection angle while preserving its ellipsoidal shape. This reshaped velocity distribution will give rise to a reshaped spatial distribution of the cloud, which can be detected in TOF measurements.

The expansion of the cloud in the presence of the SLF laser beams is calculated by employing the Fokker–Planck equation [25]. We take the linearized form of $F(v)$ from Eq. (1), this enables us to solve the Fokker–Planck equation by using the ansatz from [21]. The coefficients α_{ij} are evaluated from the calculated force at $v = 0$. The initial phase space distribution of atoms $P(x, y, v_x, v_y, t = 0)$, which is the input distribution for the Fokker–Plank equation, is defined using measured experimental values. These were determined by measuring the time evolution of the cloud's thermal expansion in a standard TOF measurement. The Fokker–Planck equation is solved numerically for different expansion times, providing the phase space distribution of atoms in the cloud for a given time. The calculated atomic density distribution is then subsequently compared to the TOF measurements.

4. SHAPE OF THE CLOUD IN THE PRESENCE OF THE SLF

In Fig. 2 we present measured [Figs. 2(b), 2(e), and 2(h)] and calculated [Figs. 2(c), 2(f), and 2(i)] atom density distributions after $\tau = 4$ ms of expansion time for three experimental configurations [Figs. 2(a), 2(d), and 2(g), respectively].

The atomic system and laser parameters used in the calculations are identical to the experimental ones, given in Section 2. The cooling laser detuning is -3.6Γ, providing a symmetrical Gaussian-shaped density distribution of the cloud at $t = 0$ ms whose standard deviation (SD) is $\sigma_x = 0.25$ mm and a velocity distribution whose SD is $\sigma_v = 0.1$ m/s.

In the configuration presented in Fig. 2(a) only the first-step SLF beams, $|0\rangle \rightarrow |1\rangle$ and $|0\rangle \rightarrow |1'\rangle$, are present. An ellipsoid shape of the cloud is measured elongated along the y-axis, Fig. 2(b). The simulated atom density distribution corresponding to this experimental geometry is shown in Fig. 2(c). The ellipsoid shape is a result of a friction force in the x direction resulting from the red-detuned first-step SLF beams. This measurement serves as a control, not only to make sure that the ellipsoid shape of the cloud is due to the first-step beams, but also to gauge the reference angle of the ellipsoid. We find the deflection angle of the major axis by fitting a 2D Gaussian to the density distribution.

By adding the second-step SLF beams, $|1\rangle \rightarrow |2\rangle$ and $|1'\rangle \rightarrow |2'\rangle$, our scheme of two pairs of two-step two-photon transitions is fully realized, Fig. 2(d). The measured atom density distribution is still ellipsoidal, but tilted by an angle $\Phi = (-12 \pm 2)^\circ$ relative to the y-axis, Fig. 2(e). This angle is a unique signature of our scheme of atoms interacting with the field of two pairs of perpendicular laser beams that drive two-step two-photon transitions. The corresponding simulation of the atom density distribution is shown in Fig. 2(f). Good agreement between measured and calculated atom density distribution is observed. The calculated angle, $\Phi_{\text{num}} = -11.6^\circ$, is within the uncertainty of the measured angle. For the density distribution in Fig. 2(f), the α_{ij} coefficients are calculated to be $(\alpha_{xx}, \alpha_{xy}, \alpha_{yx}, \alpha_{yy}) = (-3.4, 0.79, -0.20, -0.10) \times 10^{-22}$ Ns/m, giving $\alpha_R = 0.50 \times 10^{-22}$ Ns/m. In order to distinguish between the two

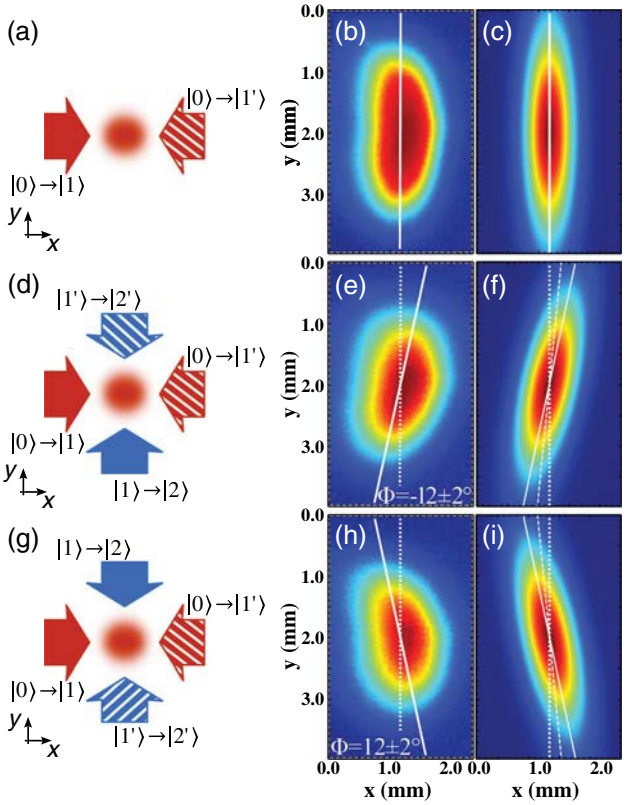

Fig. 2. Atom density distributions after TOF of 4 ms for three different configurations, (a, d, g). Corresponding experimental, (b, e, h), and numerical results, (c, f, i), are show in the same row. (b, c) Density distribution with only the first-step beams present. (e, f, h, i) Density distributions with all four beams present, hence under the influence of the SLF. Note that the two second-step beams have switched places from (d) to (g). The deflection angles of the major axes are indicated with full white lines. In panels (f) and (i) a dashed line indicates what the deflection angle would be without the SLF term in Eq. (2). See text for details.

contributions that produce the Φ_{num} angle, i.e., the trapping potential and the SLF, arising from the first and second term in Eq. (2), we calculate the density distribution without the SLF contribution ($\alpha_R = 0$). The obtained deflection angle $\Phi_{num}(\alpha_R = 0) = -5.0°$ is significantly smaller than the angle $\Phi_{num} = -11.6°$ and is indicated with a dashed line in Fig. 2(f). This is expected based on the discussion presented in Section 3, which confirms the observation of the synthetic Lorentz force in a measured cold cloud density distribution shown in Fig. 2(e).

To recheck our experimental findings we switch the two second-step SLF beams, obtaining the configuration shown in Fig. 2(g). To ensure the same alignment only the output of the fibers for the two beams are exchanged, whereas all holders, optics, and experimental parameters are left unchanged. The atom density distribution remains ellipsoidal, but it is now tilted at an angle $\Phi = (12 \pm 2)^o$ relative to the y-axis. The corresponding calculated distribution shown in Fig. 2(i) confirms the experimental result and conclusions analogous to the conclusions from the previous configuration can be made.

Another thing to note is that the tilt angle of the cloud does not increase for larger expansion times. This is due to the scalar potential, which would decrease the tilt angle if the rotating part of the force was not present. The tilt angle therefore stops increasing when the influences of these two terms on the tilt angle cancel each other. The expansion of $\tau = 4$ ms was therefore chosen because of optimal signal quality, since for smaller times the cloud is similar to the initial symmetric shape, while for larger times the signal deteriorates due to heating and diffusion.

Considering that the cyclotron frequency does not depend on the velocity of the charged particle, by analogy we expect that the deflection angle Φ in our system does not depend on the initial width of the Maxwell–Boltzmann velocity distribution of the cold cloud, i.e., on the cloud temperature. In Fig. 3 we show the measured and calculated deflection angle Φ as a function of the SD of the velocity distribution, points, and line, respectively. As mentioned in Section 3, the SD of the initial velocity distribution, σ_v, is obtained from TOF measurements without the SLF beams. In the experiment σ_v, i.e., the temperature of the cold atoms in the MOT, is easily tuned by changing the detuning of the cooling laser. The deflection angle is measured using the experimental configuration shown in Fig. 2(d), with all other experimental parameters identical to the ones used before. We can see that the measured and calculated angles agree well with the expected behavior, i.e., the deflection angle does not depend on the width of the velocity distribution almost in the entire range. Deviation of the measured angle from the calculated constant value at wider velocity distributions arises because there is a considerable number of atoms with velocities that are beyond the velocity range in which the approximation used in Eq. (1) is valid, and therefore the effect of the SLF is less pronounced. For reference, see the inset of Fig. 3 which shows the force in the y direction, $F_y(v_x, v_y = 0)$. Within the shaded area, which is from $v_x = -0.15$ m/s to $v_x = 0.15$ m/s the difference between the calculated force (green curve) and the linear approximation from Eq. (1) is below 4%. However, for a cloud with $\sigma_v = 0.15$ m/s, already 32% of the atoms have a velocity that is outside of the shaded area. For increasing σ_v this fraction will be even larger, which illustrates why the model and the experimental results differ increasingly past $\sigma_v \approx 0.15$ m/s. The values of v_x for which $F_y(v_x, v_y = 0)$ has maximum absolute values are defined by the two-photon detuning via the Doppler shift. For a larger two-photon detuning the maximum force values would be further apart and so the velocity range in which the force is linear, and thus the effective observation of the SLF is possible, could be made larger. A more complicated model could be implemented that would take into account atoms with larger velocities, as well as other effects present in the MOT, such as radiation trapping. A visible difference between the experimental TOF distribution and the numerically predicted ones in Fig. 2 is the larger width of the experimentally observed distributions along the x-axis, along which we effectively have optical molasses due to the red detuning of the first-step beams. This faster expansion is possibly a consequence of radiation trapping and very similar to the effect observed in [3]. There the authors also observed a much faster expansion of their cloud in the molasses stage than what was predicted by the Fokker–Planck equation, and this was attributed to Coulomb-like forces caused by radiation trapping. There is also additional heating not accounted for in the model, mostly due to the linewidths of the lasers which can also increase the observed width of the cloud. However, these potential additions to our model are out of scope for this paper. The model presented here is simple yet powerful in the sense that it explains and fully predicts the behavior of our system for sufficiently low atomic temperatures that are typically achieved in a MOT.

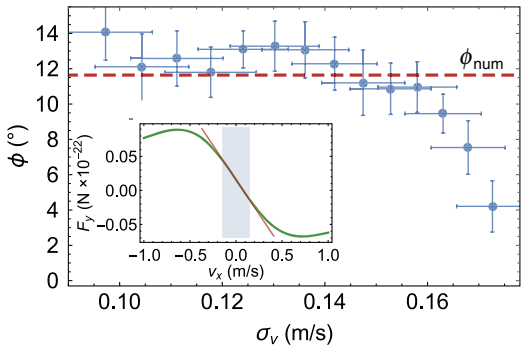

Fig. 3. Deflection angle as a function of the SD of the velocity distribution, measured (circles) and calculated (line). The inset shows the force in the y direction as a function of the velocity in the x direction, $F_y(v_x, v_y = 0)$, the region $|v_x| < 0.15$ m/s is shaded while the line shows the slope at $v_x = 0$.

5. CONCLUSION

In conclusion, we have measured the synthetic Lorentz force in an expanding cloud of cold rubidium atoms. The force is a result of the interaction of atoms with the field of two pairs of perpendicular laser beams which drive two-step two-photon transitions. The signature of the force given by our scheme is imprinted in a tilted ellipsoidal-shaped atomic cloud, measured after a given expansion time of the cloud. The experimental results show excellent agreement with the simulations of the atom density distributions. Indeed, by simulating the atom density distributions with and without the synthetic Lorentz force contribution, we can determine the contribution of

the synthetic Lorentz force in the measured deflection angle. The observed SLF has the form of the standard Lorentz force $\boldsymbol{F}_{SL}(\boldsymbol{v}) = \boldsymbol{v} \times \boldsymbol{B}^*$, where $\boldsymbol{B}^* = \alpha_R \hat{\boldsymbol{z}}$ is the effective magnetic field. Our measurement gives $\alpha_R = 0.50 \times 10^{-22}$ Ns/m, which for an ^{87}Rb ion would give an effective field $\boldsymbol{B}^*/e \approx$ 0.3 mT, or a cyclotron frequency of $\alpha_R/m = 0.35$ kHz. As stated previously, our scheme for introducing the SLF is necessarily accompanied by spontaneous emission. This will lead to radiation trapping in dense atomic clouds and therefore to an effective Coulomb force between atoms. This means that by introducing the SLF we, at the same time, introduce an effective Coulomb force in to the system. Since the effective charge as a result of radiation trapping is typically $q_{\text{eff}} \approx 10^{-4}e$ [2], the effective synthetic field scales to $B_{\text{eff}} \approx 3$T. In addition, we showed that our relatively simple model can be readily used for future experiments with synthetic fields in classical cold atom systems. Our work reinforces the analogy between a cloud of cold atoms and plasma-like systems, thus potentially opening a new direction of research based on the use of cold atoms as a classical emulator of complex classical systems in which magnetic fields play a significant role, such as a tokamak fusion reactor or a star.

Funding. Project Frequency-Comb-induced OptoMechanics; Hrvatska Zaklada za Znanost (HRZZ) (IP-2014-09-7342); QuantiXLie Center of Excellence.

Acknowledgment. We are grateful to R. Kaiser for advice and fruitful discussions.

REFERENCES

1. T. Walker, D. Sesko, and C. Wieman, "Collective behavior of optically trapped neutral atoms," Phys. Rev. Lett. **64**, 408–411 (1990).
2. D. W. Sesko, T. G. Walker, and C. E. Wieman, "Behavior of neutral atoms in a spontaneous force trap," J. Opt. Soc. Am. B **8**, 946–958 (1991).
3. L. Pruvost, I. Serre, H. T. Duong, and J. Jortner, "Expansion and cooling of a bright rubidium three-dimensional optical molasses," Phys. Rev. A **61**, 053408 (2000).
4. J. T. Mendonça, R. Kaiser, H. Terças, and J. Loureiro, "Collective oscillations in ultracold atomic gas," Phys. Rev. A **78**, 013408 (2008).
5. H. Terças, J. T. Mendonça, and R. Kaiser, "Driven collective instabilities in magneto-optical traps: a fluid-dynamical approach," Europhys. Lett. **89**, 53001 (2010).
6. J. T. Mendonça, H. Terças, G. Brodin, and M. Marklund, "A phonon laser in ultra-cold matter," Europhys. Lett. **91**, 33001 (2010).
7. J. T. Mendonça and R. Kaiser, "Photon bubbles in ultracold matter," Phys. Rev. Lett. **108**, 033001 (2012).
8. H. Terças, J. T. Mendonça, and V. Guerra, "Classical rotons in cold atomic traps," Phys. Rev. A **86**, 053630 (2012).
9. H. Terças and J. T. Mendonça, "Polytropic equilibrium and normal modes in cold atomic traps," Phys. Rev. A **88**, 023412 (2013).
10. J. D. Rodrigues, J. A. Rodrigues, O. L. Moreira, H. Terças, and J. T. Mendonça, "Equation of state of a laser-cooled gas," Phys. Rev. A **93**, 023404 (2016).
11. G. Labeyrie, F. Michaud, and R. Kaiser, "Self-sustained oscillations in a large magneto-optical trap," Phys. Rev. Lett. **96**, 023003 (2006).
12. N. Šantić, T. Dubček, D. Aumiler, H. Buljan, and T. Ban, "Experimental demonstration of a synthetic Lorentz force by using radiation pressure," Sci. Rep. **5**, 13485 (2015).
13. L. J. LeBlanc, K. Jiménez-García, R. A. Williams, M. C. Beeler, A. R. Perry, W. D. Phillips, and I. B. Spielman, "Observation of a superfluid Hall effect," Proc. Natl. Acad. Sci. USA **109**, 10811–10814 (2012).
14. M. Aidelsburger, M. Atala, M. Lohse, J. T. Barreiro, B. Paredes, and I. Bloch, "Realization of the Hofstadter Hamiltonian with ultracold atoms in optical lattices," Phys. Rev. Lett. **111**, 185301 (2013).
15. I. Bloch, J. Dalibard, and S. Nascimbene, "Quantum simulations with ultracold quantum gases," Nat. Phys. **8**, 267–276 (2012).
16. J. Dalibard, F. Gerbier, G. Juzeliunas, and P. Öhberg, "Colloquium: artificial gauge potentials for neutral atoms," Rev. Mod. Phys. **83**, 1523–1543 (2011).
17. K. W. Madison, F. Chevy, W. Wohlleben, and J. Dalibard, "Vortex formation in a stirred Bose-Einstein condensate," Phys. Rev. Lett. **84**, 806–809 (2000).
18. J. R. Abo-Shaeer, C. Raman, J. M. Vogels, and W. Ketterle, "Observation of vortex lattices in Bose-Einstein condensates," Science **292**, 476–479 (2001).
19. Y.-J. Lin, R. L. Compton, K. Jiménez-García, J. V. Porto, and I. B. Spielman, "Synthetic magnetic fields for ultracold neutral atoms," Nature **462**, 628–632 (2009).
20. M. Aidelsburger, M. Atala, S. Nascimbène, S. Trotzky, Y.-A. Chen, and I. Bloch, "Experimental realization of strong effective magnetic fields in an optical lattice," Phys. Rev. Lett. **107**, 255301 (2011).
21. T. Dubček, N. Šantić, D. Jukić, D. Aumiler, T. Ban, and H. Buljan, "Synthetic Lorentz force in classical atomic gases via Doppler effect and radiation pressure," Phys. Rev. A **89**, 063415 (2014).
22. A. Fasoli, S. Brunner, W. A. Cooper, J. P. Graves, P. Ricci, O. Sauter, and L. Villard, "Computational challenges in magnetic-confinement fusion physics," Nat. Phys. **12**, 411–423 (2016).
23. D. A. Steck, Rubidium 87 D line data, http://steck.us/alkalidata/rubidium87numbers.pdf.
24. D. Sheng, A. Perez Galvan, and L. A. Orozco, "Lifetime measurements of the 5d states of rubidium," Phys. Rev. A **78**, 062506 (2008).
25. H. J. Metcalf and P. Van Der Straten, *Laser Cooling and Trapping* (Springer, 1999).